

# Collapsars in Three Dimensions

Gabriel Rockefeller<sup>1,2</sup>, Christopher L. Fryer<sup>1,3</sup> and Hui Li<sup>2</sup>

## ABSTRACT

We present the results of 3-dimensional simulations of the direct collapse to a black hole of a rotating,  $60 M_{\odot}$ , zero metallicity, population III star. Because the structure of this star (angular momentum, density and temperature profiles) is similar to many collapsar gamma-ray burst progenitors, these calculations have implications beyond the fate of population III stars. These simulations provide a first 3-dimensional look at a realistic collapsar progenitor, and the results are very different from any previous 2-dimensional calculations. If the angular momentum of the progenitor is high, non-axisymmetric instabilities in the collapsing core cause spiral structures to form, and these structures shape later outflows. These outflows are driven by the imbalance between viscous heating and inefficient neutrino cooling and ultimately develop into a  $10^{52}$  erg explosion. Without magnetic fields, this collapse will not produce relativistic jets, but the explosion is indeed a hypernova. We conclude with a discussion of the implications of such calculations on the explosions, nucleosynthesis, neutrino flux and gravitational wave emission from the collapse of massive stars.

*Subject headings:* Gamma Rays: Bursts, Nucleosynthesis, Stars: Supernovae: General

## 1. Introduction

In the last two decades, observations have brought us a wealth of information about gamma-ray bursts (GRBs), transforming these phenomena from enigmatic curiosities to well-constrained astrophysical objects. We now know much about the immediate surroundings, host galaxies, redshift distribution, energetics, and beaming of these bursts (e.g. Sollerman et al. 2005). These observations provide a number of strong constraints on any theoretical

---

<sup>1</sup>Department of Physics, The University of Arizona, Tucson, AZ 85721

<sup>2</sup>Theoretical Division, LANL, Los Alamos, NM 87545

<sup>3</sup>Computer & Computational Sciences Division, LANL, Los Alamos, NM 87545

proposal for the engine behind these explosions. The extreme GRB energies ( $> 10^{51}$  erg) and rapid observed variability ( $\sim$  ms) led theorists to propose models that invoked accretion onto compact objects (see Narayan, Paczynski & Piran 1992), and very quickly a range of formation scenarios were proposed to produce these accretion disks (Popham, Woosley & Fryer 1999; Fryer, Woosley & Hartmann 1999).

One such model invoked the collapse of the core of a rotating massive star down to a black hole (Woosley 1993). As the rest of the star falls onto the core, its angular momentum causes it to hang up in a disk, producing a rapidly-accreting ( $\gtrsim 0.1M_{\odot} \text{ s}^{-1}$ ) black hole. It is the accretion of this stellar material that is believed to power the GRB either through neutrino/anti-neutrino annihilation or winding of magnetic fields. With the discovery of supernovae-like light-curves concurrent and cospatial with long-duration GRBs, this “collapsar” model became one of the leading engines behind this class of GRBs.

Most of the work studying the collapsar model has focused on achieving the conditions (collapse to black hole, sufficient angular momentum to form a disk, etc.) required to produce an accreting black hole engine. Very little work has focused on studying the collapse and explosion process itself. MacFadyen & Woosley (1999) made the first such calculations, using a 2-dimensional, axially-symmetric variant of Prometheus (Arnett, Fryxell & Müller 1991; Fryxell, Arnett & Müller 1991). They used simplified physics—an equation of state for electron-degenerate matter (Blinnikov, Dunina-Barkovskaya & Nadyozhin 1996) with a functional term to approximate nuclear statistical equilibrium and neutrino cooling mimicked by a single cooling term. They immediately collapsed the entire iron core to a black hole and placed an inner absorbing boundary at a radius of 50 km to mimic that black hole. They began with the helium cores of several model stars and then artificially set the angular momentum profile to ensure that the centrifugal force at collapse would be  $\leq 0.02$  times the gravitational force.

Proga et al. (2003) used the same equation of state and cooling routine in the magnetohydrodynamic code Zeus-2D to model this collapse in axial symmetry all the way down to  $1.5R_{\text{S}}$  (where  $R_{\text{S}} = 2GM/c^2$  is the Schwarzschild radius), including the effects of magnetic fields. They used the same  $25M_{\odot}$  progenitor with its ad-hoc angular momentum profile from MacFadyen & Woosley (1999). And, like MacFadyen & Woosley (1999), at the onset, they collapsed the iron core down to a black hole.

In this paper, we present the first 3-dimensional simulations of the collapsar, following the accretion of material onto the black hole down to the innermost stable circular orbit. Our progenitor is a zero-metallicity, rotating  $60M_{\odot}$  star and the rotation profile in our collapse is taken directly from the pre-collapse progenitor. We discover a number of features that the previous axially-symmetric models of collapsars did not, and could not, produce. Most

notably, we find that the initial accretion torus develops spiral wave instabilities, leading to enhanced angular momentum transport and viscous heating and the strong production of gravitational waves. In §2, we discuss our initial conditions and computational technique and the general features evident in our results. We describe the transport of angular momentum through our simulated collapsar in §3 and discuss the outflows from the central accreting torus in §4. We conclude in §5 with a discussion of the implications of these 3-dimensional accretion instabilities, including analysis of the gravitational waves produced in these models.

## 2. Code and Generic Results

Our model progenitor is a rotating  $60 M_{\odot}$  star evolved to collapse using the stellar evolution code KEPLER (Weaver et al. 1978). Figure 1 shows the density, temperature, average atomic weight ( $\bar{A}$ ), and angular velocity ( $\Omega$ ) versus enclosed mass and versus radius for this 1-dimensional simulation at collapse. The stellar evolution calculation did not include magnetic torques and the rotational velocity in the core is at the high end of possible values (for more details, see Heger et al. 2006). The peak density occurs in the inner few solar masses, and this material will collapse first, presumably forming a black hole.

Note the sharp jumps in the angular velocity (and less noticeably, but more importantly, in the density) at element boundaries in this star. This is the result of the simplistic mixing algorithm in the KEPLER code. More advanced mixing techniques for modeling convection in modern stellar evolution codes (e.g. Young et al. 2005) do not produce such sharp boundaries. The process of mapping this 1-dimensional model into three dimensions for use with our smoothed particle hydrodynamics (SPH) code tends to smooth out these boundaries slightly, but they are still quite sharp in our 3-D initial conditions and such uncertainties in our progenitor dominate the uncertainties in our calculation. That is, the  $60 M_{\odot}$  star we are currently modeling may look very different than the true structure of a  $60 M_{\odot}$  star. As stellar evolution codes improve, we hope this source of error will shrink.

The 1-dimensional structure is converted into a series of shells in our 3-dimensional SPH setup. The spacing between the shells is set to be roughly equal to the spacing between the particles within a shell. We used 2.5 million particles to model the inner  $5.6 M_{\odot}$  core of the progenitor with particle masses ranging from less than  $10^{-6} M_{\odot}$  to above  $10^{-5} M_{\odot}$ . The particles are distributed in the shells randomly (Fryer & Warren 2002) so there is no preferred axis (see Fryer, Rockefeller & Warren 2006, for details), but this does introduce perturbations in the density profile; these perturbations are roughly 10% where the density gradient is large, but less than 1% where the density is relatively flat. These perturbations will seed convection in the collapsed core.

The angular velocity is added equally into each shell with an axis along the z-axis (Fryer & Warren 2002). Hence, the angular momentum of a given particle in a shell is directly proportional to the square of its distance away from the z-axis. The specific angular momentum of each particle versus the enclosed mass at smaller radii in the progenitor is shown in Figure 2. For guidance, we also plot the specific angular momentum needed for a piece of matter to be centrifugally supported at the innermost stable circular orbit above the black hole. Here we have assumed that the black hole mass and angular momentum are set equal to the mass and angular momentum of all matter interior to the point in question. Note that over most of the mass, the distribution of angular momenta at a given radius implies that some particles (i.e. particles at higher latitudes above the equatorial plane) will fall directly into the black hole while others will hang up in a disk.

We constructed two initial models and ran two SPH simulations; the first model uses the angular momentum profile taken directly from the results of the KEPLER calculation (and shown in figure 2), while the second model uses an angular momentum profile where the magnitude of the angular momentum is reduced by a factor of 10 compared to the KEPLER results. We refer to the first model as the “rapidly-rotating” model and to the second model as the “slowly-rotating” model.

The collapse and resultant explosion of each star is modeled in one continuous simulation using the smoothed particle hydrodynamics code SNSPH (Fryer et al. 2006). SNSPH uses a tree-based self-gravity module that has been tested to accurately follow the collapse but also include the disk formation. It also includes a 3-flavor flux-limited diffusion package to simulate both neutrino cooling and the absorption of neutrinos (which affects the electron fraction of the ejecta). We use a coupled equation of state; at low densities we use the equation of state by Blinnikov et al. (1996), which was also used by MacFadyen & Woosley (1999) and Proga et al. (2003), while at high densities we employ a dense equation of state by Lattimer & Swesty (1991). To include the effects of nuclear burning, we include a nuclear statistical equilibrium package (see Herant et al. 1994; Fryer et al. 2006).

We do not model the initial formation of a neutron star at the center of the collapsing progenitor; instead, we assume that the core quickly collapses to form a black hole. To mimic this, we begin the simulation with an inner absorbing boundary. The inner boundary of the calculation is initially set at a radius of 10 km and is allowed to expand once the accreted mass and angular momentum are sufficient to move the innermost stable circular orbit around the central black hole out to larger radii. In nature, there will be a period of time before the core has collapsed to a neutron star, and this will change the initial evolution of the collapse and possibly even the explosion.

### 3. Angular Momentum Transport

The material flowing toward the inner boundary carries enough angular momentum to form a small torus at the center of the rapidly-rotating star. This torus is hot ( $> 10^{10}$  K), and gas pressure gradients inside it produce forces on par with the centrifugal force. The torus is susceptible to the formation of spiral waves (Papaloizou & Pringle 1984; Goldreich, Goodman & Narayan 1986; Li et al. 2001); a spiral structure becomes apparent at a time  $t \simeq 0.29$  s after collapse. Figure 3 shows the density in the equatorial plane of the rapidly-rotating star 0.30 s after collapse, while figure 4 shows the density 0.44 s after collapse.

The pressure gradients associated with the spiral wave are capable of transporting additional angular momentum beyond that transported by fluid viscosity. Azimuthal pressure gradients generate positive correlations between the radial and azimuthal velocities of fluid elements. Compared to a “background” fluid element not near a spiral wave, a fluid element ahead of the spiral wave will tend to move with a faster azimuthal velocity and a higher outward radial velocity, and a fluid element behind the spiral wave will tend to move with a slower azimuthal velocity and a smaller outward (or larger inward) radial velocity; both of these fluid elements transport additional angular momentum outward through the star.

To characterize the transport of angular momentum during the calculation, we follow Li et al. (2001) and calculate the variation in radial and azimuthal velocity components at points throughout the equatorial plane of the collapsar. We then use the correlations between these variations to estimate a local  $\alpha$  coefficient at each point in the flow.

We begin by calculating azimuthally-averaged radial and azimuthal velocities  $\langle v_r \rangle$  and  $\langle v_\phi \rangle$  in the midplane of the simulation at a given time. In general the actual radial and azimuthal components of the velocity at a given point differ from these average values; the radial velocity  $v_r$  differs from the average by  $\delta v_r$  ( $v_r = \langle v_r \rangle + \delta v_r$ ), and the azimuthal velocity  $v_\phi$  differs by  $\delta v_\phi$  ( $v_\phi = \langle v_\phi \rangle + \delta v_\phi$ ). The two-dimensional  $\alpha$  coefficient  $\alpha_{r\phi}$  at a given point is proportional to the product of these velocity deviations,

$$\alpha_{r\phi} = \frac{\rho \delta v_r \delta v_\phi}{P}, \quad (1)$$

where  $\rho$  is the fluid density and  $P$  is the pressure. Positive values of  $\alpha_{r\phi}$  identify regions where radial and azimuthal deviations from the average fluid velocity are positively correlated—in other words, where outward transport of angular momentum is occurring.

Figure 5 shows the value of  $\alpha$  in the equatorial plane of the rapidly-rotating collapsar, 0.30 s after collapse, while figure 6 shows the value of  $\alpha$  0.44 s after collapse. Red regions show positive correlations between azimuthal and radial velocity fluctuations and are regions of efficient outward transport of angular momentum. Blue regions show negative correlations

between azimuthal and radial velocity fluctuations and are regions of efficient inward angular momentum transport. Green regions, especially in regions of the star well outside the spiral wave, indicate angular momentum transport due solely to fluid viscosity—in our calculation, due to the artificial viscosity implemented in our code. The artificial viscosity in our code results in a value of  $\alpha \lesssim 0.01$  (depending on the particular region of the flow; fluid at larger radii shows smaller velocity fluctuations and therefore has a smaller typical  $\alpha$  value), while fluid elements near the spiral wave have values of  $\alpha \gtrsim 0.1$ . The spiral wave does produce local regions of enhanced outward angular momentum transport, but it affects only a small fraction of the material in the star and does not explain the large-scale outflows we find in our simulation (though it does help explain the asymmetric structure of those outflows).

Figure 7 shows the black hole mass  $M_{\text{bh}}$  and spin parameter  $a$  as functions of time for both the rapidly-rotating and slowly-rotating collapsar simulations. The accretion rate  $\dot{M}$  through the inner boundary of our simulation is highest around  $t = 0.28$  s after collapse, just before the spiral wave becomes clearly visible in images of the density in the equatorial plane.  $\dot{M}$  rises rapidly in the  $\sim 80$  ms leading up to the appearance of the spiral wave and drops more gradually during the following  $\sim 250$  ms. When combined with the results from figures 5 and 6, discussed above, this supports the conclusion that the presence of a spiral wave in our simulated collapsar does not significantly enhance the transport of angular momentum through the inner region of the star. Instead, enhanced viscous heating near the spiral wave helps initiate large outflows that shut off accretion onto the black hole; these outflows are described below.

#### 4. Outflows

The intense activity in the accretion torus causes considerable viscous heating and ultimately drives outflows. Figure 8 shows three snapshots in time for both the rapidly- and slowly-rotating simulations. The strong viscous heating in the rapidly-rotating case leads to outflows, but because the material is accreting through all directions (not just along the equator of rotation), the outflows differ significantly from the canonical disk outflows. With time, this model eventually halts all accretion by blowing up the star. The low-angular-momentum star does not undergo significant heating (only near the innermost stable circular orbit does viscous heating start to overcome the neutrino cooling) and the material accretes directly onto the black hole. There is very little time variation in the accretion profile.

One way to understand the outflows is to look at the Bernoulli function  $B$  for the infalling matter,

$$B = H + j^2/(2r^2) - GM_{\text{enclosed}}/r, \quad (2)$$

where  $H$ ,  $j$ , and  $r$  are, respectively, the enthalpy, specific angular momentum and radius of a piece of matter,  $G$  is the gravitational constant, and  $M_{\text{enclosed}}$  is the mass interior to that material. Blandford & Begelman (1999) have argued that if  $B$  is positive, outflows occur. Although this is not strictly true (see Abramowicz et al. 2000; Blandford & Begelman 2004, for details), the sign of the Bernouli function remains an ideal indicator of the existence of outflows. Figure 9 shows the value of this function for both our models at three different times during the simulations. Its value is nearly identical for the two models for all of the matter at the beginning of the simulation; both the enthalpy and gravitational potential energies are identical, and the rotational kinetic energy is very low. However, since angular momentum is conserved, this rotational kinetic energy grows as  $r^{-2}$  as material moves inward (versus  $r^{-1}$  for the gravitational potential energy), and it quickly becomes a dominant term. This rotational energy is then converted to heat that then drives the outflow. In our rapidly-rotating progenitor, the Bernouli number becomes positive for the bulk of disk matter out to roughly 1000 km (over 100 Schwarzschild radii). In comparison, the material in the slowly-spinning progenitor does not undergo significant heating until this matter is down at only a few times the innermost stable orbit. Even so, the viscous heating does not drive the Bernouli function above zero.

Another way to understand the outflows in the rapidly-rotating model is just through heating and cooling terms. If the cooling in an accretion flow is inefficient and there is some transport of energy, it is very difficult to accrete large amounts of matter. This is because the matter is only marginally bound. If it doesn't lose its energy through neutrino emission, it only needs to gain a small amount of energy to become unbound. If the star is not rotating rapidly, there will not be enough heating and the material will accrete directly onto the black hole; conversely, if the star is rotating sufficiently rapidly, viscous heating can drive outflows. Neutrino emission depends sensitively on the temperature and is not effective until the matter achieves high temperatures, so neutrino cooling is inefficient. In our high-angular momentum case, there is enough viscous heating transporting energy from the accreting material to the infalling material to drive considerable mass ejection.

Both MacFadyen & Woosley (1999) and Proga et al. (2003) found outflows and we expected such outflows to occur. But our outflows have very different structures than those found by these two groups. One of the reasons for this difference is their artificial choice for the angular momentum profile of the progenitor. Their choice of initial angular momentum produced a more canonical disk structure. Our initial conditions, taken directly from a stellar evolution model, lead to convection that is much closer to a classic supernova model, except that centrifugal support, not degeneracy pressure, halts the inflow.

We did not include the energy deposited through neutrino/anti-neutrino annihilation.

However, the neutrino fluxes from our simulation are quite low: below  $10^{52} \text{ erg s}^{-1}$  (Fig. 10). Using the analysis of Popham et al. (1999) as a guide, we would expect less than  $10^{50}$  erg of energy to be deposited by neutrino annihilation. Given that viscous heating ultimately drives a  $10^{52}$  erg explosion in our rapidly-rotating model, neutrino annihilation can reasonably be neglected.

We also do not include the effects of magnetic fields. The SPH technique does have an artificial viscosity which deposits energy locally, mimicking the “alpha-viscosity” transport of angular momentum that we might expect from a turbulent magnetic field. But even in our extremely altered structures near the black hole, it is possible that some sort of dynamo will produce global magnetic fields that drive a jet along the rotation axis like that seen by Proga et al. (2003). Without magnetic fields, we do not produce this jet (and hence, do not produce a gamma-ray burst); this calculation is still incomplete and we are far from understanding all the features of such collapse models.

## 5. Implications

We have presented the results from two collapsar simulations of a  $60 M_{\odot}$  star. These are the first simulations of the collapsar model in three dimensions. The rapidly-spinning star (using the angular momentum profile of the stellar evolution model) quickly forms a small accretion torus which eventually ejects considerable mass in a disk-driven wind. This ejecta drives a hypernova-like explosion with a total explosion energy above  $10^{52}$  erg. Our second simulation, with one-tenth the total angular momentum, accreted directly onto the nascent black hole without any mass ejection. The only evidence of this collapse will be the weak neutrino and gravitational wave signal (see below). The difference in fate of these two collapsing stars highlights the sensitivity of the collapse to the angular momentum profile in the core (a factor of ten in angular momentum can make the difference between a fizzle and a  $10^{52}$  erg explosion).

Our 3-dimensional simulations paint a very different picture than what was obtained from 2-dimensional simulations. Both the realistic stellar structure and the fact that we are modelling the collapse in three dimensions lead to the development of spiral-wave instabilities; fluid viscosity ultimately transports energy outward through the star and drives a hypernova-like explosion. The “disk” formed in these calculations does not fit the structure of any analytic studies performed to date on GRB disks. This means that our understanding of how collapsars produce GRB jets as well as the nature of the nucleosynthesis, neutrino emission and gravitational wave emission from these stars may be substantially different than previous predictions. These changes will depend sensitively on the angular momentum,



and much more work must be done to fully understand collapsars.

3.3s into the simulation, the ejecta from this viscosity-driven explosion is moving at velocities in excess of  $5,000 - 10,000 \text{ km s}^{-1}$  (Fig. 11) with some ejecta moving faster than  $30,000 \text{ km s}^{-1}$ . At such high velocities, the shock is strong enough to drive explosive nucleosynthesis well into the star (see, for example, Maeda & Nomoto 2003; Nomoto et al. 2005; Fryer et al. 2006). The spiral wave instability is imprinted on the motion of the ejecta and it is far from symmetric (Fig. 12). The entropy of this shocked material is plotted in figure 13. Some of the material reaches high entropies characteristic of hypernova explosions (a small amount of matter reaches entropies in excess of  $100 k_B$  per nucleon) and these entropies will alter the signature of the nucleosynthetic yield (see Maeda & Nomoto 2003; Fryer et al. 2006, for details). It is likely that this explosive nucleosynthesis will dominate over disk nucleosynthesis (e.g. Surman, McLaughlin & Hix 2006) for our simulation and collapsar models like it. We defer investigation of the exact yields of this explosion to a later paper.

Some of the ejecta will have low electron fractions. The electron neutrino and anti-neutrino fluxes very quickly evolve to be nearly identical, but until the explosion cuts off the accretion, the anti-neutrino energies are roughly 20% higher (Fig. 10) and hence will be absorbed preferentially over the electron neutrinos. If the neutrino fluxes could reset the electron fraction of the ejecta, the higher electron anti-neutrino absorption rate would produce an electron fraction below 0.5. However, bear in mind that (1) the neutrino energies may be different with better transport schemes, and (2) this enhanced emission occurs primarily when the compact remnant is still likely to be a neutron star. If our simulation included the emission from electron capture in this neutron star, the electron neutrino flux would be higher. Although there are some differences between the neutrino light-curves in this calculation and that of a typical core-collapse supernova, most of these differences occur because we have not included the neutron star prior to collapse.

One of the new discoveries in this study was the development of instabilities in the disk. The hot, self-gravitating torus of material around the central black hole is susceptible to the formation of spiral waves, and these waves facilitate enhanced outward transport of angular momentum through the star. The instabilities that develop in the disk lead to mass motion and neutrino emission asymmetries that can produce gravitational wave emission. The frequency of these oscillations is a function of the motion of the spiral wave instability. Although at the inner edge of the disk, oscillation periods can be less than 1 ms, in practice, the period has frequencies in the 100-1000 Hz regime. Using the formulism described in Fryer, Holz & Hughes (2004) for SPH data, we have calculated the amplitude of the gravitational wave emission from both mass-motion and neutrino asymmetries. Figure 14 shows the signal from mass-motion for our rapidly- and slowly-rotating models. The maximum amplitude of

the signal, at the time of initial collapse, can be nearly 15 times larger for this collapsar model than the strongest signal arising from the rotating models in Fryer et al. (2004).

Comparing figure 15 to the work of Fryer et al. (2004), we find that the gravitational wave signal from asymmetric neutrino emission is not significantly higher than what we would expect from supernovae. In the case of our rapidly-spinning star, this is because the mass outflows limit the amount of material that piles up around the black hole, causing the neutrino luminosity to drop (Fig. 10). In the case of the slowly-spinning star, the neutrino luminosity is never very asymmetric. Even so, the neutrino gravitational wave signal is at least as strong as that for supernovae (and could be a factor of 5 higher in some cases).

With such results, we find it unlikely that LIGO or advanced LIGO can detect the gravitational wave signal from collapsars out to 1 Mpc, making this class of GRBs (possibly all long-duration GRBs), with their low occurrence rate, a poor source for gravitational wave detectors. However, we are not considering all the potential gravitational wave emission mechanisms in the collapsar model; for example, we do not consider black hole ringing, although Fryer et al. (2002) argued this would be small. We also do not model the actual black hole formation, and this will change the signal considerably.

**Acknowledgments** This work was carried out under the auspices of the National Nuclear Security Administration of the U.S. Department of Energy at Los Alamos National Laboratory under Contract No. DE-AC52-06NA25396. This work was funded in part by a DOE SciDAC grant DE-FC02-01ER41176, by a NASA grant SWIF03-0047, and by the National Science Foundation under Grant No. PHY99-07949.

## REFERENCES

- Abramowicz, M. A., Lasota, J.-P. & Igumenshchev, I. V. 2000, MNRAS, 314, 775
- Arnett, D., Fryxell, B., & Müller, E. 1989, ApJ, 341 L63
- Blandford, R. D. & Begelman, M. C. 1999, MNRAS, 303, L1
- Blandford, R. D. & Begelman, M. C. 2004, MNRAS, 349, 68
- Blinnikov, S. I., Dunina-Barkovskaya, N. V. & Nadyozhin, D. K. 1996, ApJS, 106, 171
- Fryer, C.L. & Warren, M.S. 2002, ApJ, 574, L65
- Fryer, C. L., Holz, D. E. & Hughes, S. A. 2004, ApJ, 609, 288
- Fryer, C. L., Rockefeller, G. & Warren, M. S. 2006, ApJ, 643, 292

- Fryer, C. L., Woosley, S. E. & Hartmann, D. H. 1999, *ApJ*, 526, 152
- Fryxell, B., Arnett, D., & Müller, E. 1989, *ApJ*, 367, 619
- Goldreich, P., Goodman, J., & Narayan, R. 1986, *MNRAS*, 221, 339
- Heger, A., et al. 2006, in preparation
- Herant, M., Benz, W., Hix, W. R., Fryer, C. L. & Colgate, S. A. 1994, *ApJ*, 435, 339
- Lattimer, J.M. & Swesty, F.D. 1991, *Nucl. Phys. A*, 535, 331
- Li, H., Colgate, S. A., Wendroff, B. & Liska, R. 2001, *ApJ*, 551, 874
- MacFadyen, A. I. & Woosley, S. E. 1999, *ApJ*, 524, 262
- Maeda, K. & Nomoto, K. 2003, *ApJ*, 598, 1163
- Narayan, R., Paczynski, B. & Piran, T. 1992, *ApJ*, 395, L83
- Nomoto, K., Tominaga, N., Umeda, H., Maeda, K., Ohkubo, T., Deng, J. 2005, *Nuc. Phys. A*, 758, 263
- Papaloizou, J. C. B. & Pringle, J. E. 1984, *MNRAS*, 208, 721
- Popham, R., Woosley, S. E. & Fryer, C. L. 1999, *ApJ*, 518, 356
- Proga, D., MacFadyen, A. I., Armitage, P. J. & Begelman, M. C. 2003, *ApJ*, 599, L5
- Sollerman, J., Östlin, G., Fynbo, J.P.U., Hjorth, J. Fruchter, A. & Pedersen, K. 2005, *New Astron.*, 11, 103
- Surman, R., McLaughlin, G. C. & Hix, W. R. 2006, *ApJ*, 643, 1057
- Weaver, T. A., Zimmerman, G. B. & Woosley, S. E. 1978, *ApJ*, 225, 1021
- Woosley, S. 1993, *ApJ*, 405, 273
- Young, P. A., Meakin, C., Arnett, D., & Fryer, C. L. 2005, *ApJ*, 629, L101

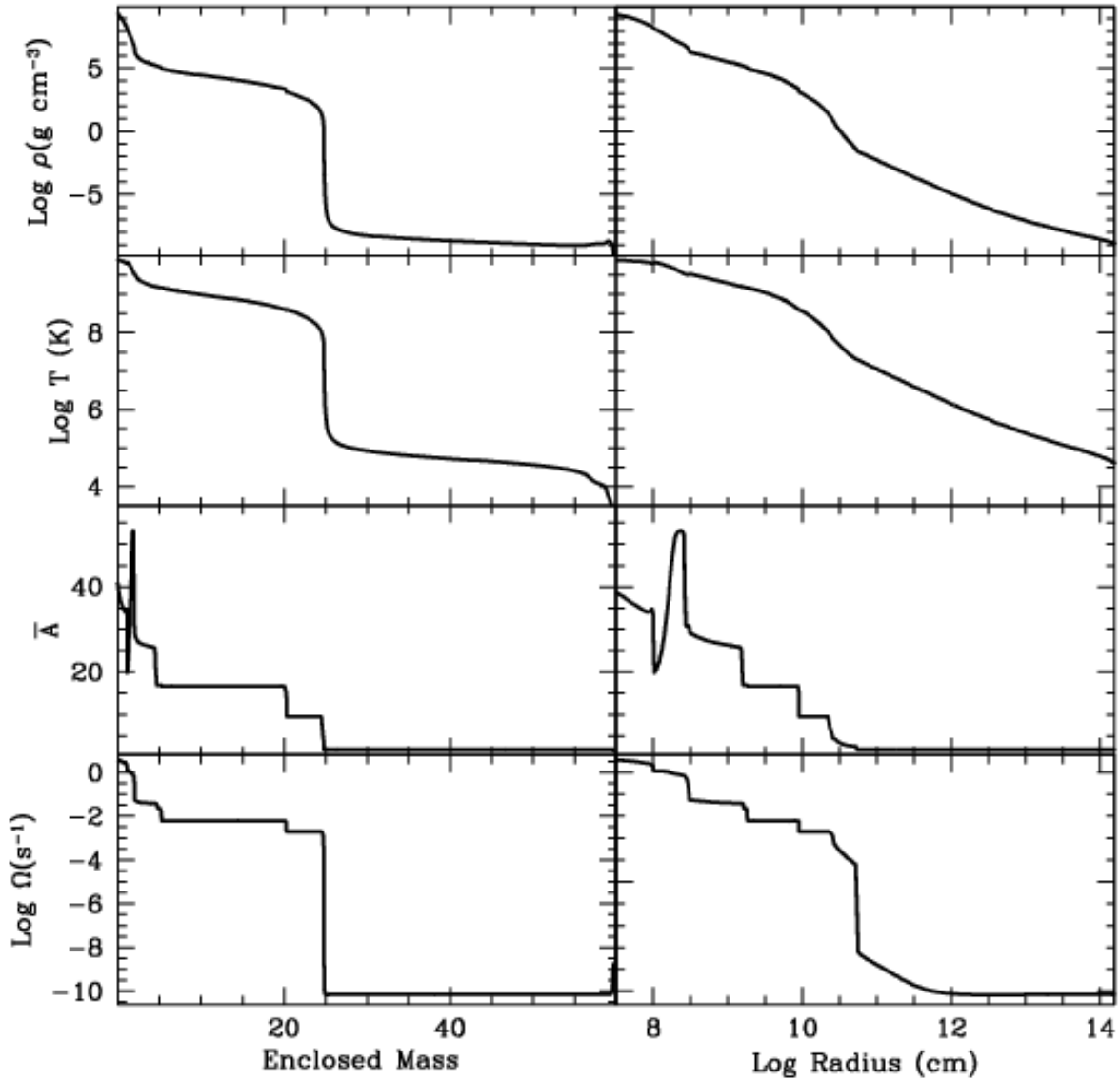


Fig. 1.— Density, temperature, average atomic weight ( $\bar{A}$ ), and angular velocity ( $\Omega$ ) versus enclosed mass and versus radius for our 1-dimensional progenitor. The peak density occurs in the inner few solar masses, and this material will collapse first, presumably forming a black hole. The sharp jumps in the angular velocity (and less noticeably, but more importantly, in the density) at element boundaries in this star are caused by the simplistic mixing algorithm in the KEPLER code. Such jumps affect the collapse and are an indication of the uncertainties in the initial progenitor that plague all stellar collapse simulations.

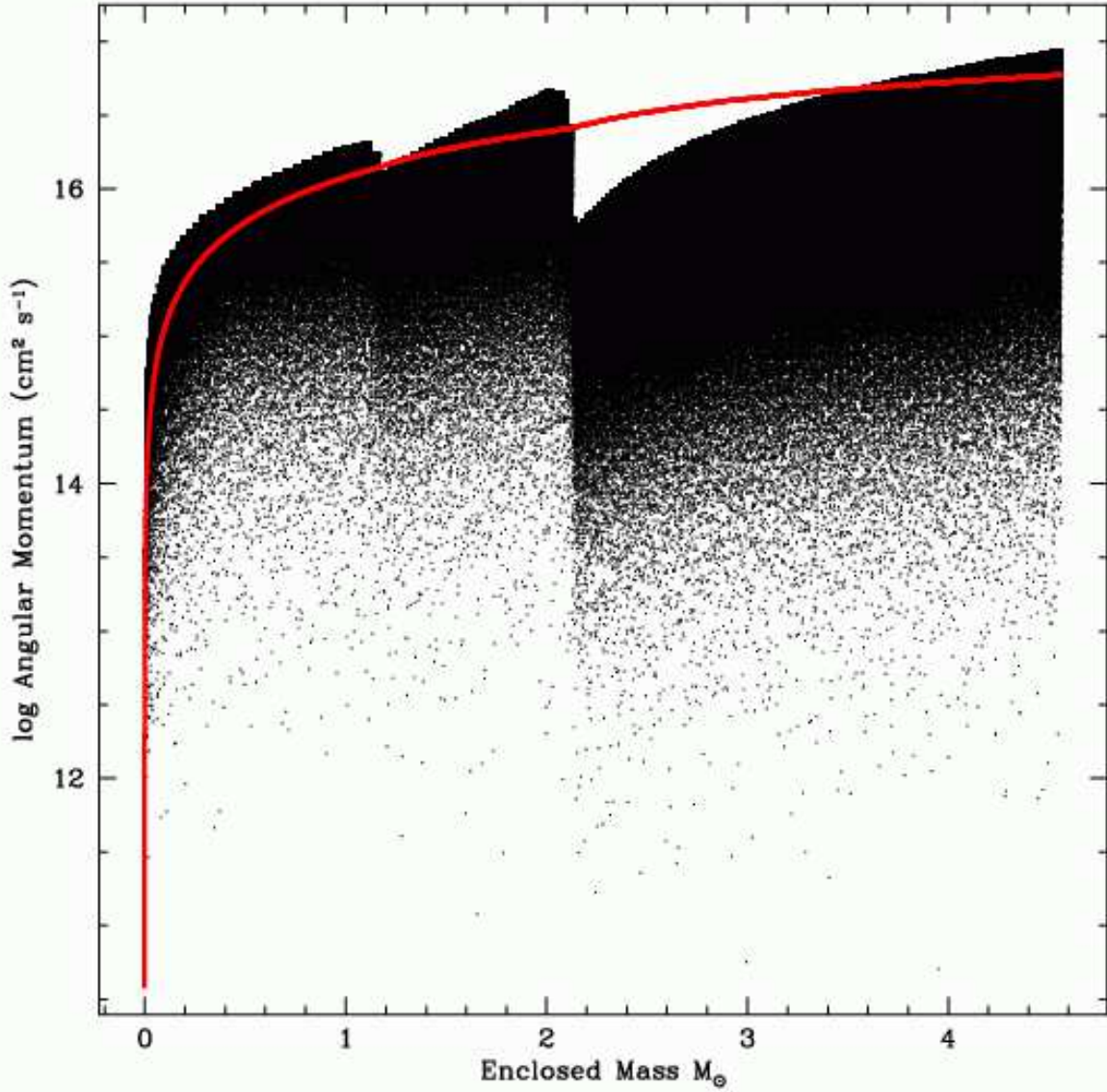


Fig. 2.— Specific angular momentum versus enclosed mass for our 3-dimensional setup. The red line shows the angular momentum needed for a piece of matter to be centrifugally supported at the innermost stable circular orbit above a black hole. Here we have assumed the black hole mass and angular momentum are set to the mass and angular momentum of all matter interior to the point in question. Note that over most of the mass, the distribution of angular momenta at a fixed radius implies that some particles will fall directly into the black hole while others will hang up in a disk.

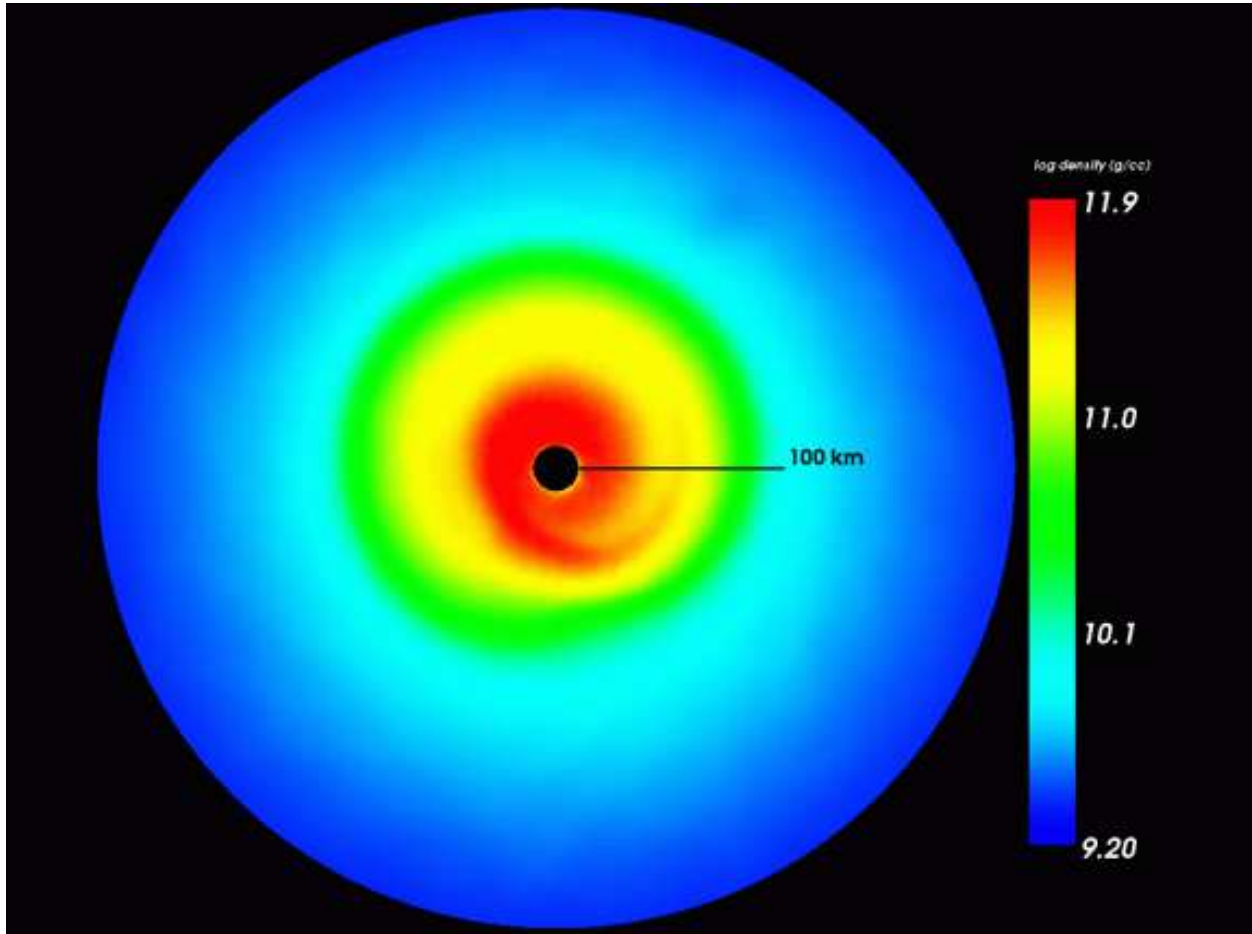


Fig. 3.— The matter density in the equatorial plane of the rapidly-rotating collapsar simulation, 0.30 seconds after collapse. The spiral wave becomes visible near the center of the collapsar  $\sim 0.29$  s after collapse.

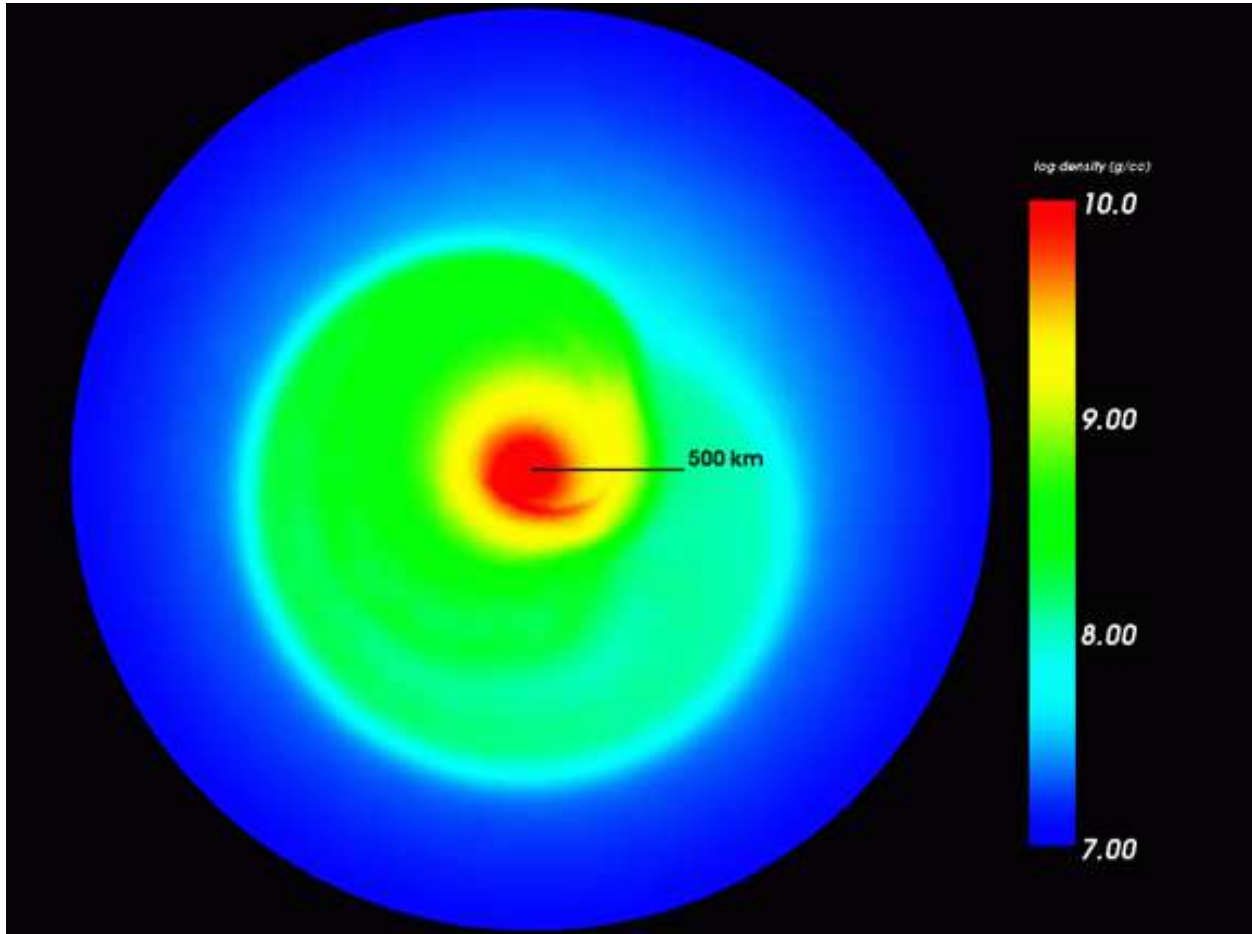


Fig. 4.— The matter density in the equatorial plane of the rapidly-rotating collapsar simulation, 0.44 seconds after collapse. The spiral wave forms near the center of the collapsar 0.29 s after collapse and moves outward through the star.

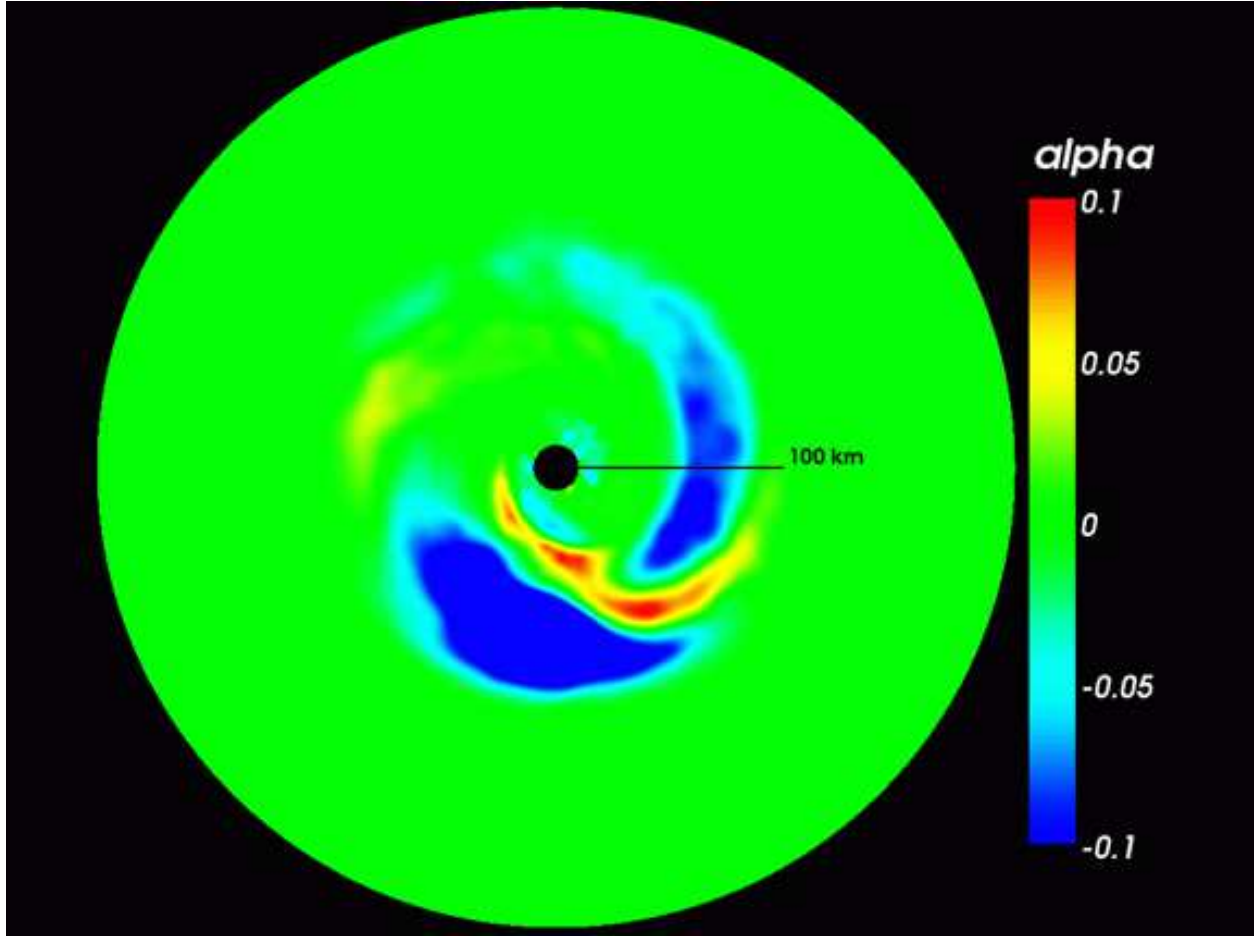


Fig. 5.— The two-dimensional  $\alpha$  coefficient  $\alpha_{r\phi}$  in the equatorial plane of the rapidly-rotating collapsar simulation, 0.30 seconds after collapse. The red regions (i.e. regions of large outward angular momentum transport) lie along the leading edges of the spiral wave. The color scale was restricted to the range  $|\alpha_{r\phi}| \leq 0.1$  to more clearly illustrate small spatial variation in  $\alpha_{r\phi}$ ; the actual range in the data is  $-0.4 \leq \alpha_{r\phi} \leq 0.1$ .



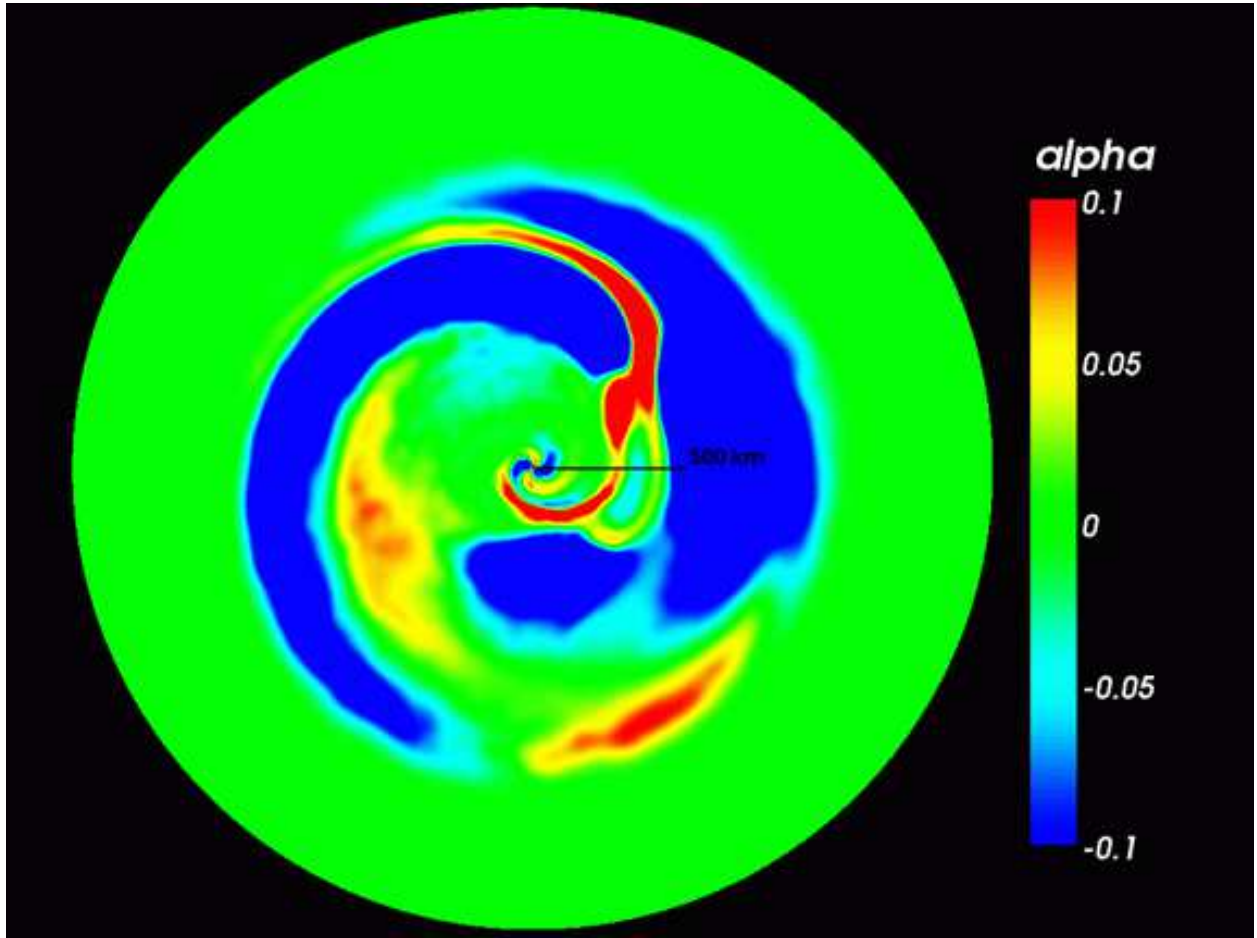


Fig. 6.— The two-dimensional  $\alpha$  coefficient  $\alpha_{r\phi}$  in the equatorial plane of the rapidly-rotating collapsar simulation, 0.44 seconds after collapse. The red regions (i.e. regions of large outward angular momentum transport) lie along the leading edges of the spiral wave. The color scale was restricted to the range  $|\alpha_{r\phi}| \leq 0.1$  to more clearly illustrate small spatial variation in  $\alpha_{r\phi}$ ; the actual range in the data is  $-0.6 \leq \alpha_{r\phi} \leq 0.4$ .

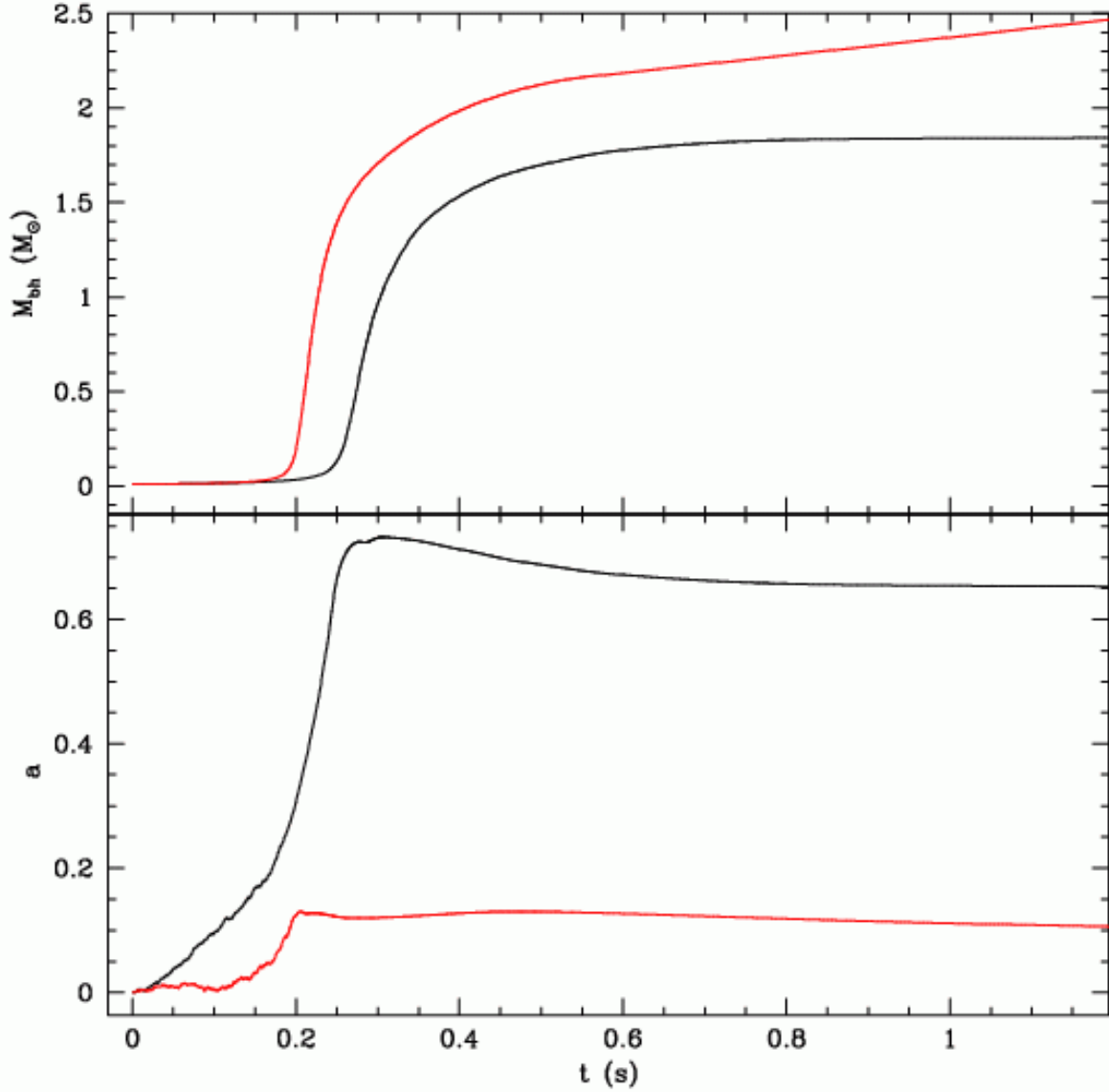
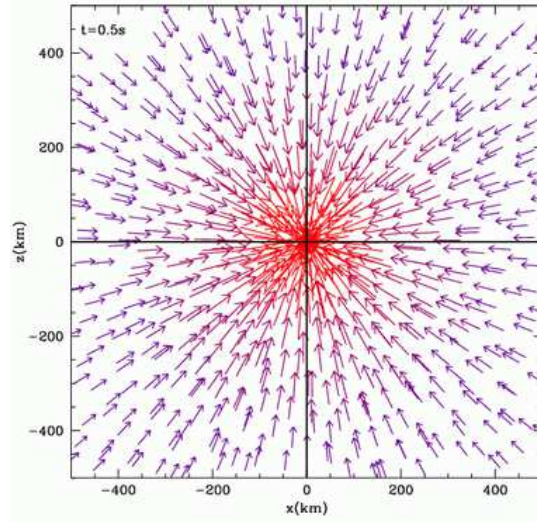
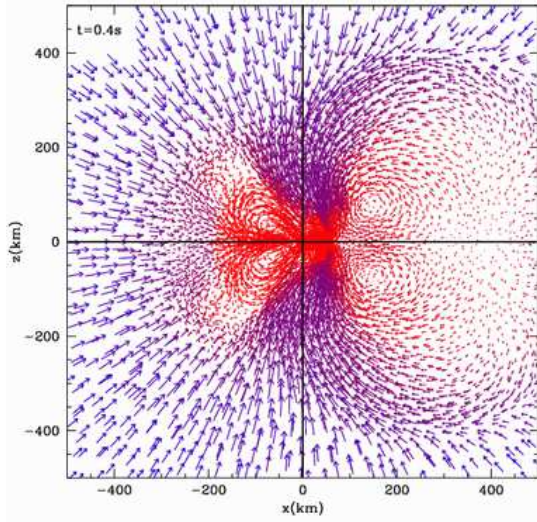
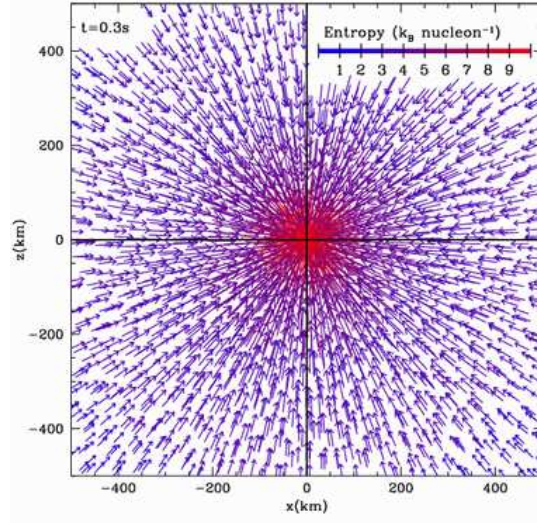
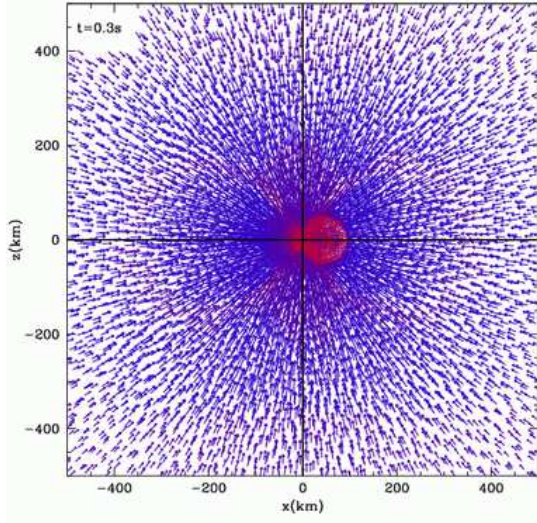


Fig. 7.— The black hole mass  $M_{\text{bh}}$  and spin parameter  $a$  as functions of time for the rapidly-rotating (black line) and slowly-rotating (red line) collapsars. A spiral wave forms in the center of the rapidly-rotating model, 0.29 s after collapse; viscous heating near the spiral wave initiates outflows and eventually prevents further accretion.



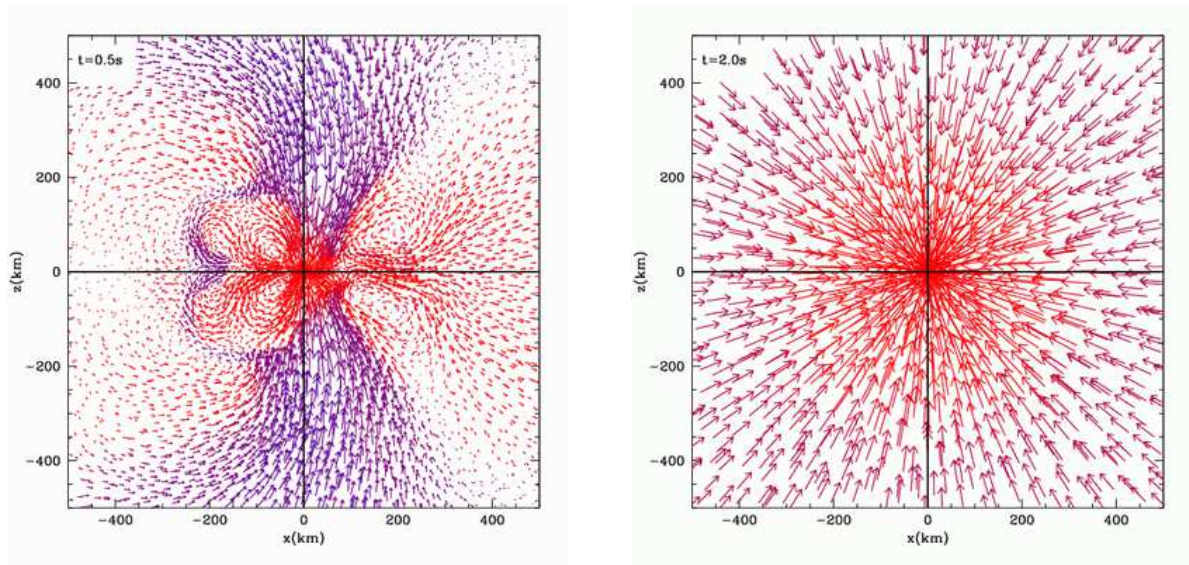


Fig. 8.— Slices in the  $x$ - $z$  plane of both our rapidly-rotating (left) and slowly-rotating (right) models. We show three separate snapshots in time for both models. The color coding denotes the entropy, and the vectors denote velocity magnitude (length) and direction. Although most of the material initially falls radially inward in our rapidly-rotating case, angular momentum causes this material to hang up in a torus, and heating ultimately produces strong outflows. Note how different these outflows are from canonical disk outflows. The convective motions in this outflow are more akin to a standard supernovae than an accretion disk. The only difference is the fact that centrifugal support, not the hard surface of a neutron star, is halting the inflow of material. By 0.5 s the outflow is well beyond 500 km. For the slowly-rotating model, the radial inflow persists to times later than 2.0 s after collapse.

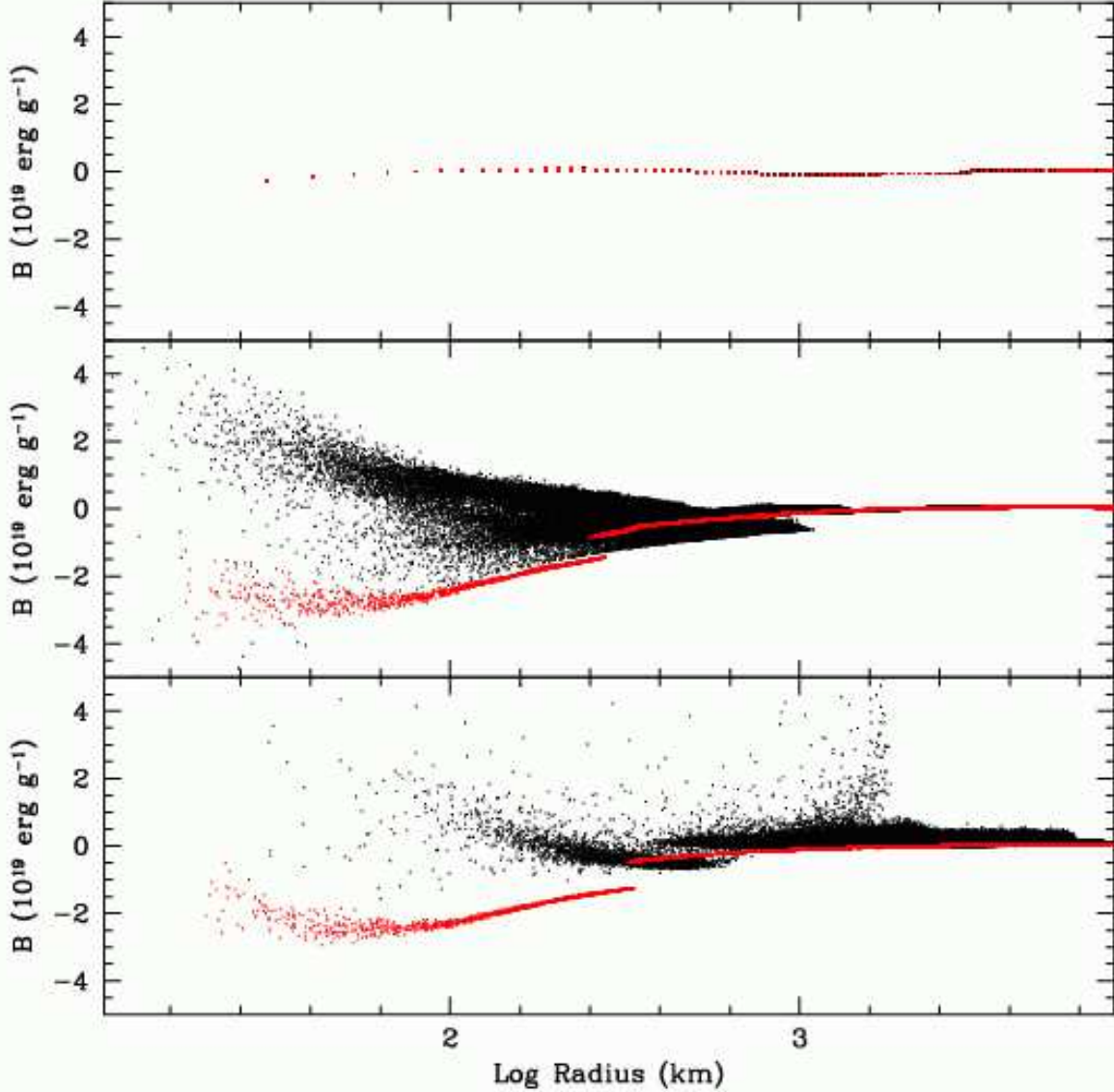


Fig. 9.— The value of the Bernouli function (eq. 2) as a function of radius at three different snapshots in time. The rapidly-rotating (black) and slowly-rotating (red) models are plotted together. Note that at time  $t = 0$ , the values of both models are nearly identical. This is because both the enthalpy and gravitational potential energies for these two models are initially identical, and the rotational energy is not a dominant term until the matter collapses. Since the rotational energy (if angular momentum is conserved) increases inversely with the square of the radius, it quickly becomes more important and viscous heating drives outflows. For the rapidly-rotating model, the heating starts to overcome neutrino cooling as far out as 1000 km. For the slowly-rotating model, viscous heating only starts to overcome the neutrino cooling at a few times the innermost stable circular orbit, and it is never able to drive the Bernouli function positive.

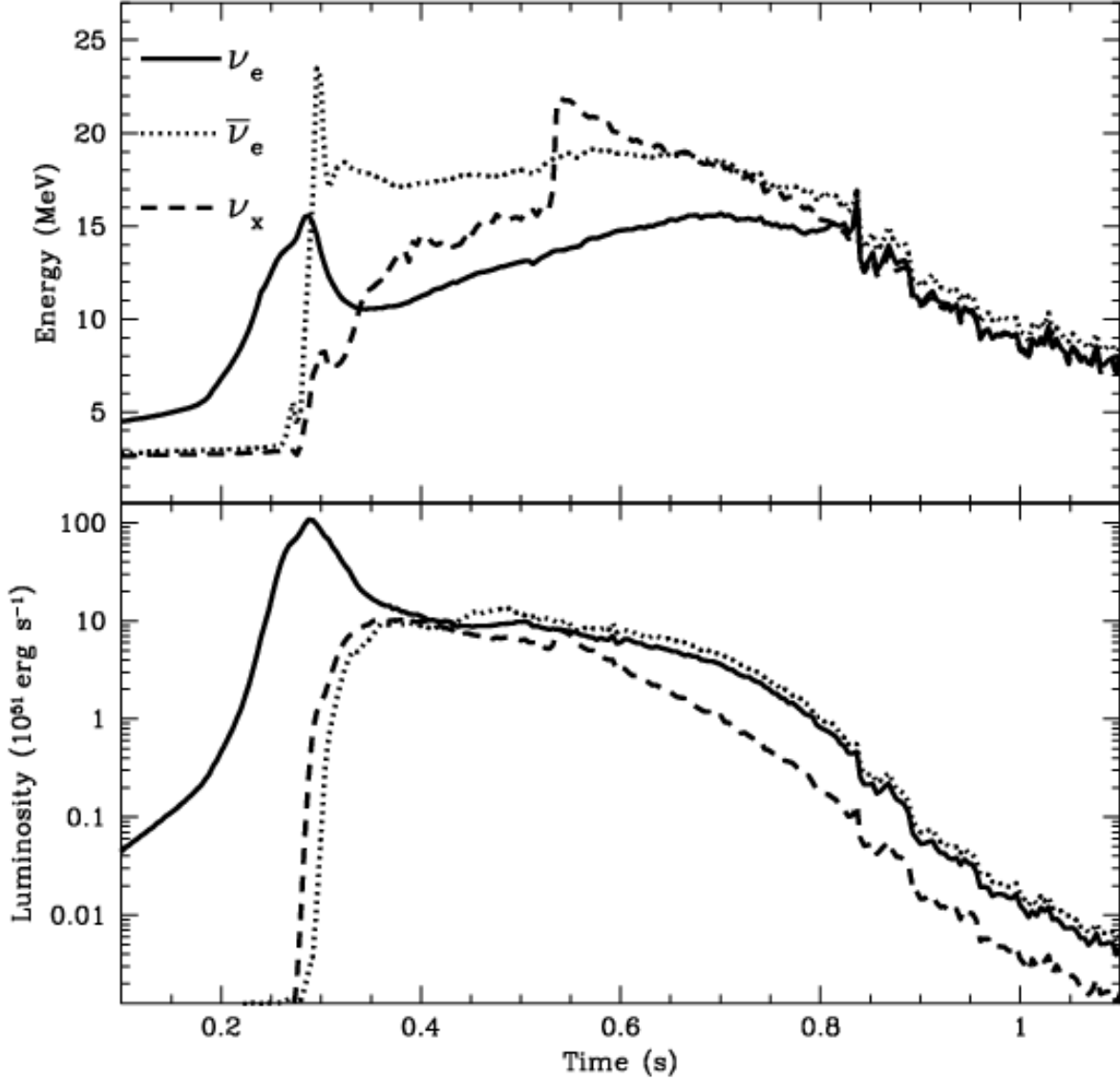


Fig. 10.— The neutrino energy (top) and neutrino luminosity (bottom) as a function of time in our simulation for the three neutrino flavors followed in our simulation: electron neutrino ( $\nu_e$  - solid), electron anti-neutrino ( $\bar{\nu}_e$  - dotted), and  $\mu$  and  $\tau$  neutrinos and anti-neutrinos ( $\nu_x$  - dashed). Note that the electron neutrino and anti-neutrino luminosities and energies are nearly equal at late times, suggesting that the neutrino flux will strive to set the electron fraction to 0.5 at these times. The electron fraction is critical in determining the yield from matter ejected in this collapse.

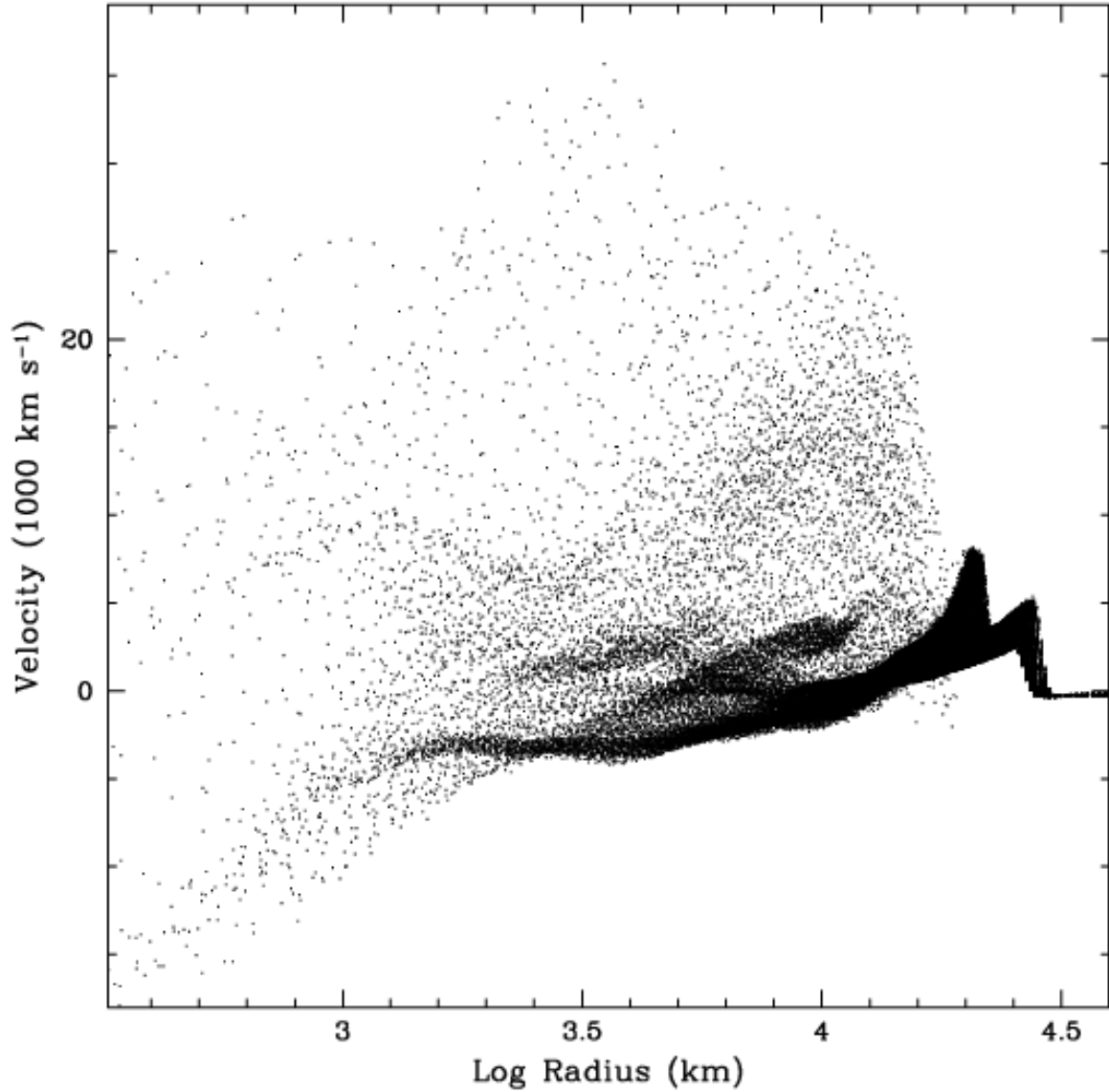


Fig. 11.— Velocity of a wedge of material (material with  $|y|/r < 0.08$ ) as a function of radius 3.3s after collapse. Two primary shocks exist, one near  $5,000 \text{ km s}^{-1}$  and the other near  $8,000 \text{ km s}^{-1}$ . But some material with velocities above  $20,000 \text{ km s}^{-1}$  also exists. These high velocities will cause much of the star to go through explosive nucleosynthesis, probably producing considerable amounts of  $^{56}\text{Ni}$ .

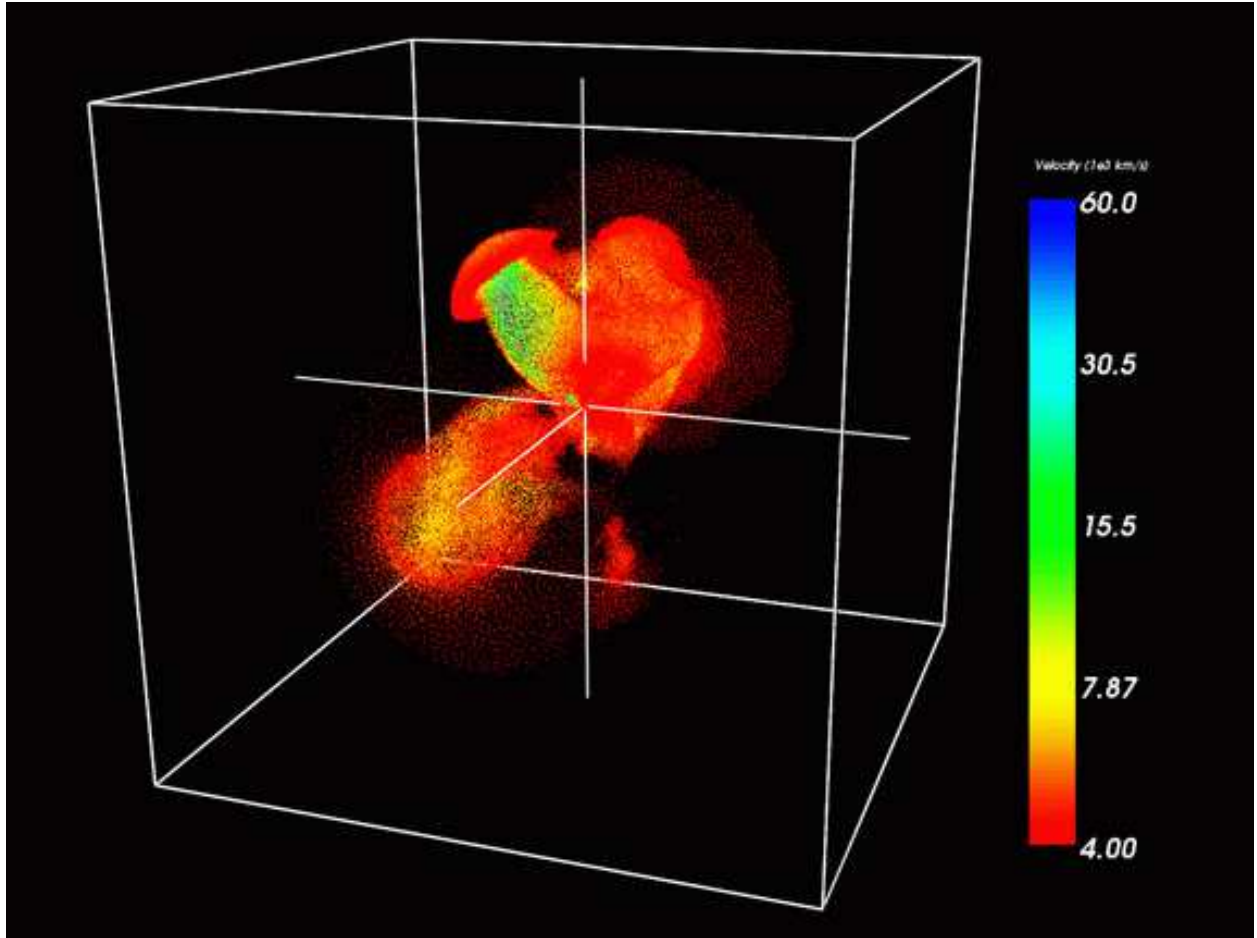


Fig. 12.— SPH particles in the rapidly-rotating collapsar simulation, selected and colored by radial velocity, 7.8 seconds after collapse. Only particles with outward radial velocities greater than  $4000 \text{ km s}^{-1}$  are shown in the image; areas containing no visible particles represent regions where the gas is moving outward relatively slowly, or actually falling inward toward the central black hole. The half-side-length of the bounding box is  $5.8e3 \text{ km}$ .



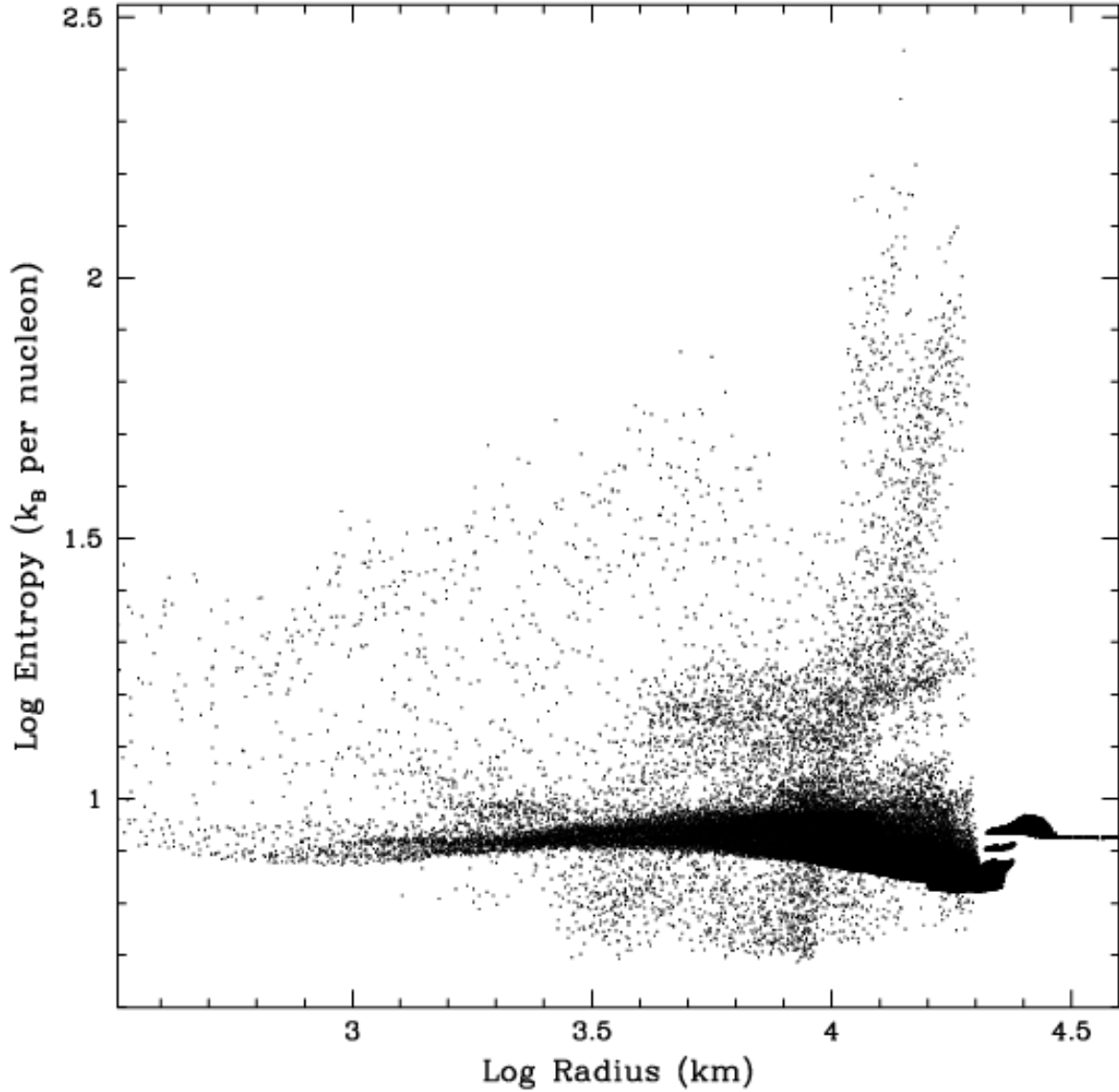


Fig. 13.— Entropy of a wedge of material (material with  $|y|/r < 0.08$ ) versus radius of the ejecta 3.3 s after collapse. Although much of the matter has normal/low entropies ( $\sim 8$ – $10 k_B$  per nucleon), some of the matter achieves extremely high entropies (in excess of  $100 k_B$  per nucleon). Such high entropies will alter the nucleosynthetic yields of this matter.

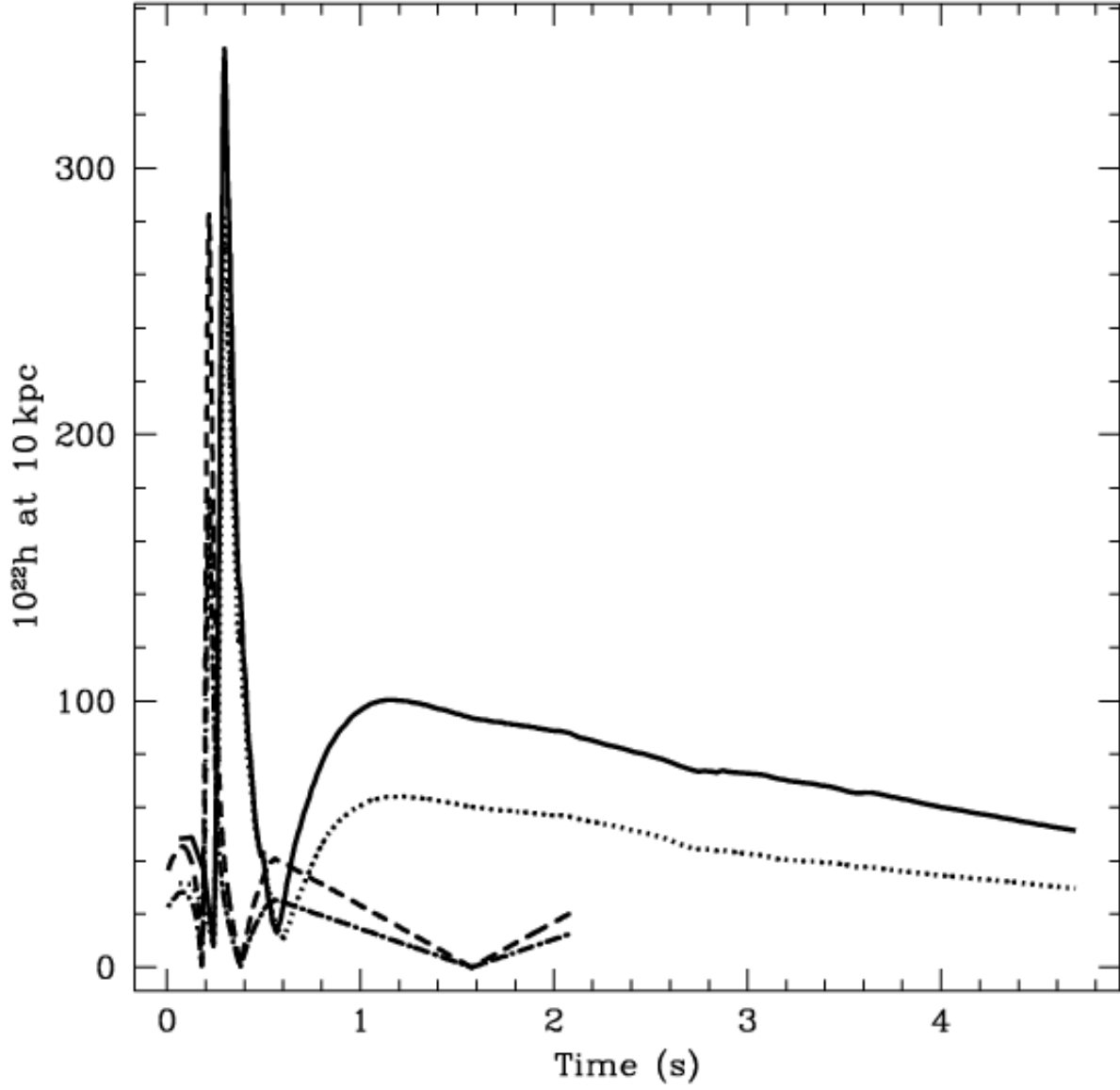


Fig. 14.— Angle-averaged wave amplitude of the gravitational wave emission arising from mass motions as a function of time for the rapidly-rotating (solid:  $\langle h_{\times}^2 \rangle^{1/2}$ , dotted:  $\langle h_{+}^2 \rangle^{1/2}$ ) and slowly-rotating (dashed:  $\langle h_{\times}^2 \rangle^{1/2}$ , dot-dashed:  $\langle h_{+}^2 \rangle^{1/2}$ ) simulations.

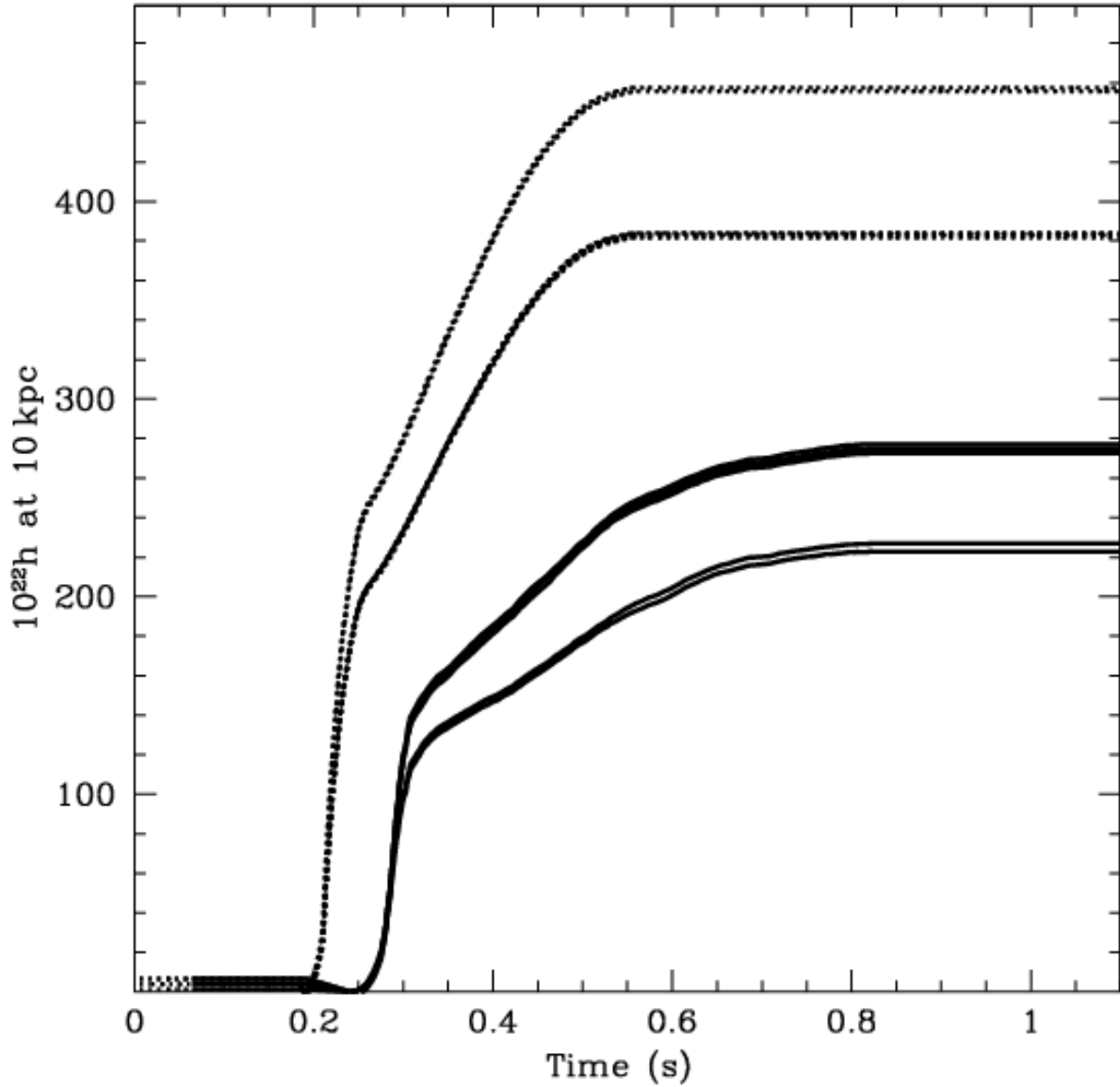


Fig. 15.— The amplitude of the gravitational wave emission arising from neutrino asymmetries as a function of time for the rapidly-rotating (solid) and slowly-rotating (dotted) simulations. The multiple lines denote different viewing angles and bracket the range of possible signals.